Redox-dependent formation of a viral amyloid and functional impact

Frank Gondelaud[1*†], Alexandre Lalande[2†], Giulia Pesce[1], Christophe Bignon[1], Patrick Fourquet[3], Denis Ptchelkine[1], Nicolas Brouilly[4], Pierre-Yves Lozach[5], Denis Gerlier[2], Cyrille Mathieu[2*] and Sonia Longhi[1*]

[1]Laboratoire Architecture et Fonction des Macromolécules Biologiques (AFMB), UMR 7257, Aix Marseille University and Centre National de la Recherche Scientifique (CNRS), 163 Avenue de Luminy, Case 932, 13288 Marseille, France

[2]CIRI, Centre International de Recherche en Infectiologie, Univ Lyon, Inserm, U1111, CNRS, UMR5308, Université Claude Bernard Lyon 1, Ecole Normale Supérieure de Lyon, 69007, Lyon, France

[3]INSERM, Centre de Recherche en Cancérologie de Marseille (CRCM), Centre National de la Recherche Scientifique (CNRS), Marseille Protéomique, Institut Paoli-Calmettes, Aix Marseille University, 27 Bvd Leï Roure, CS 30059, 13273 Marseille, France

[4]Aix Marseille Université, CNRS, IBDM, Marseille, France

[5]University of Lyon, INRAE, EPHE, IVPC (Infections Virales et Pathologie Comparée), 69007, Lyon, France

[†]Authors contributed equally to this work.
*Corresponding authors: sonia.longhi@univ-amu.fr; cyrille.mathieu@inserm.fr; frank.gondelaud@univ-amu.fr

Author Contributions: F.G., A.L., G.P., C.M. and S.L. designed the experiments; F.G. performed all the *in-vitro* experiments except for the mass spectrometry analyses that were performed by P.F.; A.L. performed transfection, live imaging microscopy studies and ROS quantification; C.B. and F.G. generated all the constructs except for the constructs of the W^{HeV} proteins with an N-terminal *tc* tag that were generated by A.L.; D.P. provided guidance on NS-EM studies; G.P. carried out the ultramicrotomy experiments and related EM analyses with the help and guidance of N.B.; D.G. provided guidance on transfection and confocal microscopy studies and suggested to perform experiments with FKBP; P.Y.L provided guidance on the use of the *tc* tag; F.G, A.L, G.P., P.F, C.M. and S.L analyzed the data; F.G. wrote the first draft of the manuscript and generated all the figures except for Figure 4 that was jointly generated by A.L., F.G. and G.P. and Figure 5 that was generated by A.L. and F.G.; F.G., A.L., C.M., D.G. and S.L generated the final version of the manuscript, and all the authors reviewed and edited it.

Competing interests: The authors declare no competing interest.

Keywords: Henipavirus, amyloid fibrils, innate immune response, cysteine, intrinsically disordered proteins

Abstract

The Hendra and Nipah viruses (HeV and NiV) are zoonotic biosafety level-4 pathogens within the *Paramyxoviridae* family. We previously showed that their W proteins form amyloid-like fibrils *in vitro*. Here, we demonstrate that W also forms fibrils *in cellula* and that cysteine residues are crucial in dictating the ability of W proteins to fibrillate. The cysteine oxidation state acts as a switch to generate either amorphous aggregates or flexible fibrils. Ectopic expression of W^{HeV} induces an oxidative stress and W^{HeV} fibrils were observed in the nuclei of different cell lines, with fibrillation being impaired by cysteine substitutions. Finally, nuclear fibrils are associated with an impairment of the NF-κB pathway in W^{HeV} transfected cells. This work provides experimental evidence for the ability of *Henipavirus* W proteins to fibrillate in transfected cells and the first clues on their functional impact.

Significance Statement

Nipah and Hendra viruses are severe pathogens infecting humans and livestock, classified among the 8 highest priorities for research by the WHO. The W protein, along with the V protein, is a virulence factor responsible for antiviral response inhibition and we demonstrate here that its fibrillation into amyloid-like fibrils occurs in the nucleus of transfected cells, with their formation being dependent of the redox state of the W cysteine residues. The sole transfection of W provokes the production of reactive oxygen species, creating a suitable environment for the fibrils to form. Finally, we show that W fibrils enhance the repression of the antiviral response, thus pointing to W fibrillation as a new promising antiviral target.

Introduction

Hendra (HeV) and Nipah viruses (NiV) are members of the *Henipavirus* genus, within the *Paramyxoviridae* family of the *Mononegavirales* order. They are zoonotic viruses responsible for severe encephalitis and respiratory illness with a high case fatality, and as such, they are considered high-priority targets by the WHO. Since the identification of HeV and NiV in humans and fruit-bats from the *Pteropus* genus (1, 2), new species have been described including the Cedar virus identified in bats (3), the Langya virus identified in patients, bats and shrews (4, 5) and two novel species in shrews (6). Transmission from bats to humans occurs through the consumption of raw date palm sap (NiV) or from close contact with infected livestock, particularly horses (HeV) and pigs (NiV) (7). Interhuman transmissions also occurred in the case of NiV Bangladesh strain (8). Henipavirus outbreaks are unpredictable but occur almost every year with a high case fatality rate (70-90%) while no antiviral therapeutic nor vaccine is currently available (1, 9). For these reasons, HeV and NiV are biosafety level-4 pathogens.

Henipaviruses, like all paramyxoviruses, are enveloped viruses containing a non-segmented single-stranded RNA genome of negative polarity (-ssRNA) tightly associated with the nucleoprotein (N). The encapsidated RNA is the template of the viral RNA-dependent RNA polymerase (L) that, in association with the phosphoprotein (P), ensures the transcription and the replication of the viral genome (1). Beyond the P protein, the P gene also drives the synthesis of the V, W, and C proteins. The V and W proteins are produced through a co-transcriptional editing mechanism involving the addition of one (V) or two (W) non-templated G nucleotides at the editing site of the P messenger (2). In NiV-infected cells, equimolar proportions of P, V, and W transcripts are detected in the early stage of infection while the quantity of V and W transcripts increases as the infection progresses (10). The W proteins of HeV and NiV contain a nuclear localization sequence (NLS) in their unique C-terminal domain (CTD) leading to their nuclear accumulation in infected cells. Nuclear importation relies on binding to importins α3 and α4 and, to a lower extent, to importin α1 and α7 (11). W, along with P and V, also contains a nuclear export signal (NES) in its N-terminal domain (NTD) ensuring its export to the cytoplasm of infected cells *via* a Crm-1-dependent nuclear export (12, 13). Inhibition of Crm-1 in transfected cells leads to the accumulation of NiV V in the nucleus demonstrating its dual localization despite its predominant localization in the cytoplasm in untreated cells (13). Since W is almost found in the nucleus of infected cells, the NLS overcomes the NES (10, 14).

The V and W proteins are virulence factors implicated in the inhibition of the antiviral response by binding several key cellular proteins (1, 10, 15–17). The lack of the V and W proteins in the non-pathogenic Cedar virus due to the absence of the RNA editing site, concomitantly to the absence of pathogenicity associated with this virus in humans further supports this view (3, 18). W proteins bind and sequester in the nucleus STAT1 through their NTD, common to P and V, inhibiting the interferon response (1, 16, 19). Additionally, the CTD of the W proteins binds 14-3-3 proteins through its serine 449 leading to 14-3-3 protein nuclear accumulation. This accumulation enhances the nuclear export of p65, reducing its ability to interact with its promoter targets, thereby inhibiting the NF-κB-induced proinflammatory response (20). Binding to 14-3-3 also provokes cell apoptosis through a less defined mechanism (21).

We previously showed that the W proteins from HeV and NiV (W^{HeV} and W^{NiV}) are intrinsically disordered and can aggregate in an amyloid-like fashion (22). W^{NiV} and W^{HeV} contain cysteine residues implicated in W dimerization (22). We hypothesized that cysteine residues could impact the fibrillation ability of W proteins. Using various biophysical approaches and site-directed mutagenesis, we demonstrate here that the cysteine oxidation state dictates the ability of W^{HeV} and W^{NiV} to fibrillate. We also show that W^{HeV} forms fibrils in the nucleus of transfected cells with the redox-dependance of the process being retained also in the cellular context. Finally, we shown that W fibrils enhance the repression of the NF-κB-mediated antiviral response, suggesting a role of W fibrils in viral escape from the innate immune response.

Results

Cysteines are responsible for the formation of oligomeric species and of a compact conformation

W^{HeV} and W^{NiV} contain four and six cysteine residues respectively, three of which are shared by both proteins (**Figure 1A**). Since the W proteins are intrinsically disordered (22) and thus possess a large solvent-accessible surface area, we hypothesized a strong reactivity of these residues. The proteins, purified in reducing and denaturing conditions, were incubated at 37°C in the presence of urea to avoid their spontaneous aggregation into amyloid-like fibrils while enabling cysteines to undergo natural oxidation, presumably *via* the formation of intra- and/or interchain disulfide bridges. This pre-incubation in urea of the proteins will thereafter be referred to as "oxidative preincubation" (**Supplementary Figure 1**).

In addition to the monomer (vertical violet line in **Figure 1B** and peak I in **Supplementary Figure 2A**), size exclusion chromatography (SEC) analysis of the W proteins during oxidative preincubation showed the fast formation of dimeric species (vertical yellow line in **Figure 1B**), consistent with previous observations (22), as well as the formation of higher-order oligomers within 24h for W^{HeV} and 48h for W^{NiV} (vertical grey line in **Figure 1B**). The nature of the oligomeric species of W^{HeV} was disentangled by mass photometry, which showed the co-existence in the sample of monomeric, dimeric, trimeric and likely tetrameric species (**Supplementary Figure 2B**). Additionally, a species (vertical pink line in **Figure 1B** and peak II in **Supplementary Figure 2A**) that eluted at a volume slightly larger than that of the initial monomeric species can be detected upon incubation. For W^{HeV}, non-reducing SDS-PAGE and mass spectrometry analysis revealed that this species corresponds to a monomeric form of the protein (**Supplementary Figures 2C** and **2D**), and its elution volume indicates a more compact conformation (**Figure 1B**).

While W^{HeV} oligomerization does not seem to evolve further after 48h of oxidative preincubation, in the case of W^{NiV} it continues to progress even after 4 days (**Figure 1B**). Addition of DTT during the preincubation in urea (for 72h for W^{HeV} and for 96h for W^{NiV}), led to the disappearance of both the oligomers (grey line in **Figure 1B**) and the compact conformation (pink line in **Figure 1B**) indicating

that they are both redox-sensitive and result from the formation of inter- and intramolecular disulfide bonds, respectively (**Figure 1B**).

Cysteine oxidation is required for W^{HeV} and W^{NiV} fibrillation

The aggregation of W^{HeV} and W^{NiV} was followed by turbidity as well as by means of thioflavin T (ThT) fluorescence measurements (**Figure 1C-F**). In these experiments, as well as in all the ensuing experiments unless differently stated, the W proteins were pre-incubated for different periods in urea to promote the formation of oligomers as in **Figure 1B**. After this oxidative preincubation period, urea was removed and the aggregation process was monitored for 2 hours at 37°C in a urea-free buffer (see procedure in **Supplementary Figure 1**). Urea removal without an oxidative preincubation, *i.e.* at time 0, led to the formation of macroscopically visible insoluble aggregates (**Figure 1C** and **1D**) that eventually sedimented and that did not bind ThT (**Figure 1E** and **1F**). By contrast, oxidative preincubation of W proteins for at least 24h led to a clear solution (**Figure 1C** and **1D**) containing species that bind ThT (**Figure 1E** and **1F**), suggesting the formation of fibrillar structures. After one or two additional preincubation days (48h and 72h in **Figures 1C** and **1E**), neither the turbidity nor the fluorescence emission evolved significantly for W^{HeV}, coincidentally with the arrest of oligomerization as observed by analytical SEC (**Figure 1B**). In contrast, W^{NiV} ThT binding continued to gradually increase (**Figure 1F**), mirroring the evolution of its oligomerization (**Figure 1B**). The nature of the aggregates formed with or without an oxidative preincubation period was assessed by negative-staining electron microscopy (NS-EM). Grids were prepared after the 2 hours of incubation over which the aggregation measurements were carried out (**Figure 1G**). The insoluble aggregates that are formed without an oxidative preincubation have an amorphous nature, while W^{HeV} and W^{NiV} preincubated in oxidative conditions give rise to amyloid-like fibrils (**Figure 1G**).

The constant increase of W^{NiV} oligomers content over time can be ascribed to its higher content in cysteine residues that keep reticulating the protein. The balance between fibril nucleation and elongation is low in the case of W^{HeV}, as judged from the fact that it rapidly forms fewer, though longer fibrils than W^{NiV}. On the contrary, the cysteine residue oxidation degree strongly promotes the extent of W^{NiV} nucleation which eventually forms massive amounts of short fibrils as shown by NS-EM (**Figure 1G**). The ThT fluorescence intensity seems to correlate with the nucleation extent rather than with fibril size.

W^{NiV} and W^{HeV} fibrils have the particularity of being not straight but rather highly curved (**Figure 1G**). Measurements of the contour length of W^{HeV} fibrils observed in micrographs revealed that 24h of oxidative incubation led to the longest fibrils, up to 830 nm in these experimental conditions, with an average size of 273 nm (**Figure 1H**). The proportion of short fibrils increased with the incubation time, presumably reflecting fibril fragmentation that regularly occurs in amyloid fibrils. After 72h of incubation, the average length of fibrils dropped to 179 nm (**Figure 1H** and **Supplementary Table 1**).

Taken together, these observations suggest that disulfide bonds formation is the initial step in the fibrillation of both W^{HeV} and W^{NiV} proteins, since non-oxidized monomeric species are poorly able to undergo fibrillation. We thus hypothesized that the oligomers could promote the formation of fibrillar structures. This was explored further by focusing on W^{HeV} in light of its lower cysteine content and its faster oligomerization compared to W^{NiV}. Since 48h of incubation of W^{HeV} represents a good compromise between solubility and fibril length, and because the oligomerization process does not progress further after this period, this oxidative preincubation time was selected for the following analyses of W^{HeV} fibrillation.

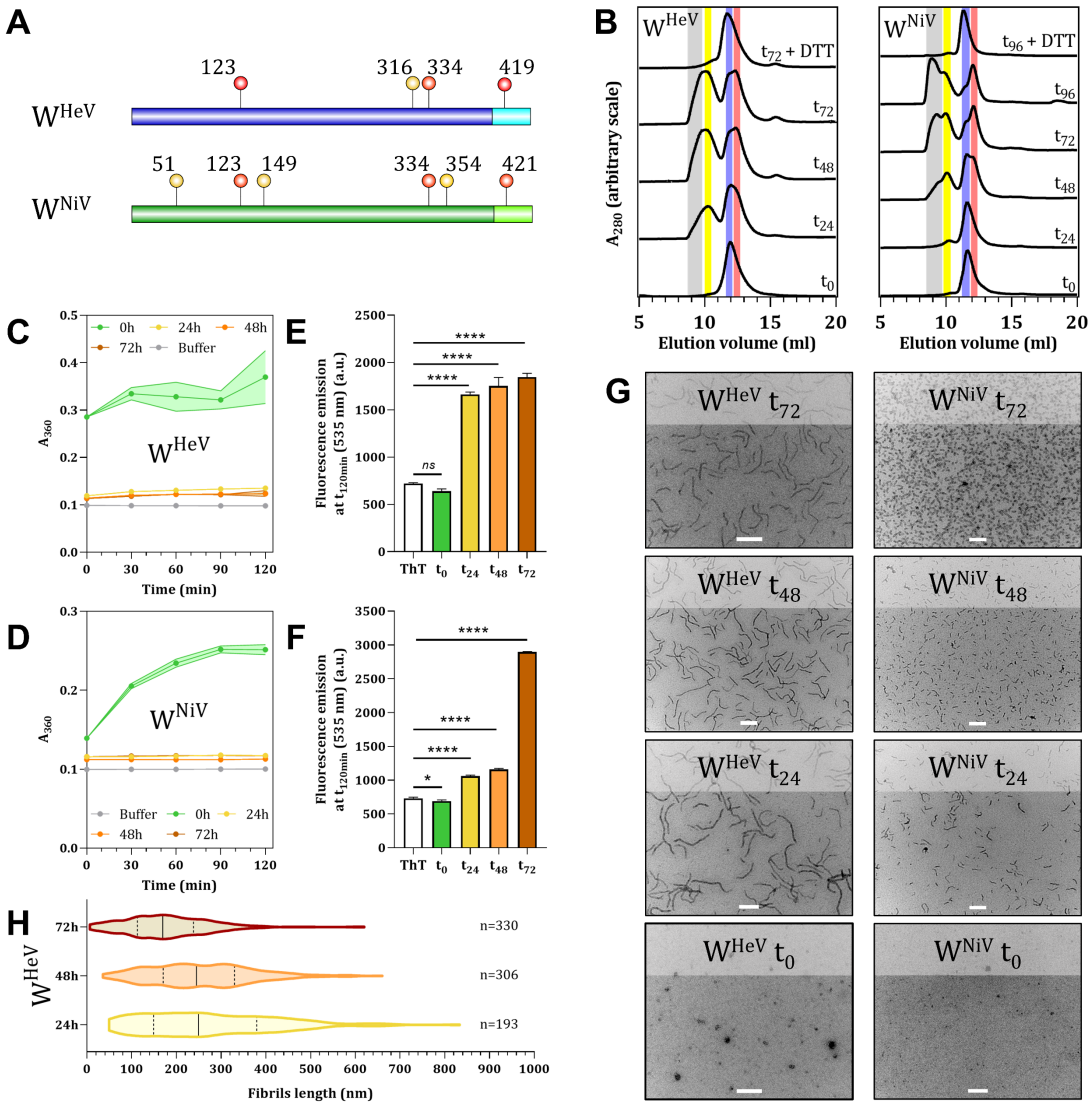

Figure 1: Cysteine residues oxidation of W^{HeV} and W^{NiV} is required to promote their fibrillation. A) Location of cysteine residues in W^{HeV} (blue) and W^{NiV} (green) proteins. Conserved Cys are indicated in red. Dark colors: N-terminal domain (NTD), bright colors: C-terminal domain. Schemes have been made with IBS software (23). **B)** Analytical SEC of the W proteins after different preincubation times in oxidative condition at 37°C in the presence of urea, and either in the absence (t_0, t_{24}, t_{48}, t_{72}, and t_{96}) or in the presence of DTT (t_{72} or t_{96} + DTT). The vertical grey, yellow, and violet bars correspond to the oligomeric, dimeric and monomeric species, respectively. The vertical pink bar corresponds to the more compact monomeric form. **C)** Turbidity and **E)** ThT fluorescence measurements of W^{HeV} preincubated for 0 (green), 24 (yellow), 48 (orange), and 72 hours (brown) at 37°C in urea and then buffer exchanged to remove urea. Shown is also the fluorescence of ThT alone (white). Panels C and D show the average values and s.d. as obtained from n=4 independent measurements. Statistical analysis was made with a one-way ANOVA, Dunnett's test, ns: not significant, ****: $p<0.0001$. The shaded region in C) corresponds to the error bar. **D)** Turbidity and **F)** ThT fluorescence measurements of W^{NiV} preincubated or not. The legend is the same as for C) and D). **G)** NS-EM micrographs of W^{HeV} and W^{NiV} incubated for 120 min at 37°C in urea-free buffer without preincubation (0h) or following a preincubation of 24, 48 and 72h at 37°C in urea. **H)** W^{HeV} fibril contour length measurements from NS-EM micrographs after 24, 48, and 72h of preincubation. Median and quartiles are represented as continuous and dotted lines, respectively. The number of fibril length measurements is indicated for each condition. Scale bar: 200 µm.

The involvement of cysteine residues in W^{HeV} fibrillation was confirmed by generating a variant where the four cysteine residues were all substituted to serine residues (W^{HeV} $C^{all}S$) (**Figures 2A-D**). As expected, W^{HeV} $C^{all}S$ remains monomeric after 48h of oxidative preincubation in urea (**Figure 2A**). After urea removal, insoluble aggregates that do not bind ThT were detected as in the case of the wild-type (WT) protein not subjected to the oxidative preincubation (**Figure 2B** and **2C**). Under these conditions, NS-EM confirmed the sole presence of amorphous aggregates (**Figure 2D**). Furthermore, the addition of DTT on preincubated W^{HeV} immediately after urea removal, *i.e.,* at t_0, led to a progressive decrease in solubility over the 120 min of incubation (**Figure 2B**). After 120 min, ThT binding was weaker in the presence of DTT (red bar) than in its absence (orange bar), but not as low as that observed with the non-incubated WT protein (green bar) or with the W^{HeV} $C^{all}S$ variant (blue bar) (**Figure 2C**). NS-EM micrographs taken after 120 min of incubation in the presence of DTT showed the co-existence of rare and small fibrils, and of amorphous aggregates (**Figure 2E**).

Formation of W^{HeV} fibrillar structures is not reversible upon reduction

To assess whether the fibrillation process was reversible, W^{HeV} was incubated 48h in oxidative conditions thus enabling disulfide bond formation, and then allowed to assemble into amyloid-like fibrils for 2h after urea removal, before the addition of DTT (**Figure 2F-K**). Aggregation measurements and NS-EM were performed after two extra hours ($t_{2h + 2h}$) after DTT addition. As expected, these experiments showed decreased solubility and ThT binding (**Figure 2F** and **2G**) and the presence of massive clusters of fibrillar structures that were not observed in the absence of DTT (*cf.* **Figure 2H** and **2I**).

After 24h of incubation in the presence of DTT, the samples were centrifuged and the pellet was resuspended and deposited on an NS-EM grid (**Figure 2J**). NS-EM showed large filamentous structures of micrometric scale consisting of clustered fibrils (**Figure 2J**) indicating that the fibrillation process is not fully reversible through reduction, though a limited fraction of W^{HeV}, presumably monomers detached from the fibrils, became insoluble and amorphous according to the aggregation measurements made just after 2h of incubation. Thus, while disulfide-bridged oligomers and/or the redox-sensitive compact conformation, *i.e.,* species II in **Supplementary Figure 2A**, play a critical role in fibrils nucleation, once fibrils have formed, a redox-independent mechanism maintains monomers together. Disulfide bonds regulate as well fibrils assembly while their reduction in mature fibrils causes random association of W^{HeV} leading to the formation of fibrillar clusters.

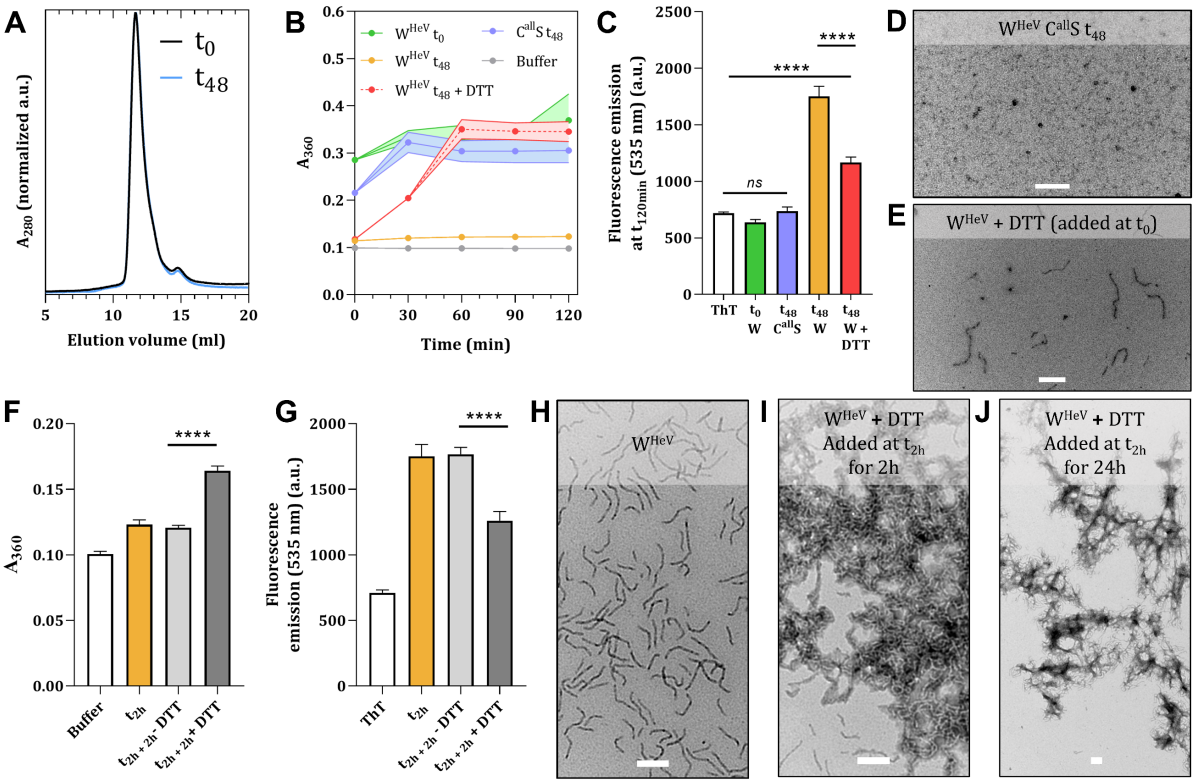

Figure 2: Cys-to-Ser substitution abrogates W^{HeV} fibrillation and aggregation in fibrillar structures cannot be reversed. A) Analytical gel filtration of W^{HeV} $C^{all}S$ preincubated for 48h (t_{48h}, blue) or not (t_{0h}, black) in urea. **B)** Turbidity and **C)** ThT fluorescence measurements of W^{HeV} $C^{all}S$ (blue) and of the wild-type W^{HeV} protein in the presence of DTT (red), both preincubated for 48h. Non-incubated (0h, green) and preincubated for 48h (orange) wild-type W^{HeV} data are shown for comparison. NS-EM micrographs were taken after two hours of incubation of W^{HeV} $C^{all}S$ preincubated for 48h in urea **(D)** and of wild-type W^{HeV} in the presence of DTT added after urea removal **(E)**. **F)** Turbidity and **G)** ThT fluorescence measurements of W^{HeV} preincubated for 48h and after 2h of incubation following urea removal (orange), and after 2 extra hours in the presence (dark grey) or absence (light grey) of DTT. NS-EM micrographs of W^{HeV} preincubated for 48h in urea and after 2h of incubation following urea removal *plus* 2 extra hours in the absence **(H)** or presence **(I)** of DTT. W^{HeV} was preincubated for 48h in urea and then for 24h in urea-free buffer in the presence of DTT. The solution was centrifuged and the resuspended pellet **(J)** were observed by NS-EM. Panels C and G also display the fluorescence of ThT alone (white). Panels B,C,F, and G show the average values and error as obtained from n=4 independent measurements. Statistical analysis was made with a Student t-test, ns: not significant, ****: $p<0.0001$. The shaded region in B) corresponds to the error bar. Scale bar: 200 µm.

Dimeric species initiate fibrillation

In order to identify the minimal molecular assembly required for fibril nucleation, W^{HeV} triple Cys to Ser variants were generated allowing only dimerization of the protein, although in different proportions as observed by SEC analysis (**Figure 3A**). After 48 h of preincubation in oxidative conditions and a 2 h-incubation after urea removal, the four variants were able to bind ThT (**Figure 3B**) and to fibrillate (**Figure 3C**) indicating that the sole presence of dimeric species is sufficient to promote W^{HeV} fibrillation. At first glance, the nucleation extent, *i.e.* the number of fibrils observed on micrographs, seems to be at least partly related to the initial amounts of dimers observed in SEC analysis. Indeed, the W^{HeV} $C123^{only}$, $C316^{only}$, and $C419^{only}$ variants, which display considerable amounts of dimers, give rise to micrographs characterized by a high density of relatively short fibrils. Conversely, the W^{HeV} $C334^{only}$ variant, which weakly dimerizes, displays attenuated nucleation as

judged from the presence of rare fibrils in micrographs (**Figure 3C**). These observations strongly support the implication of dimeric species in the nucleation step of W^{HeV} fibrillation.

To further confirm the relation between fibril nucleation and oligomerization, we first artificially generated oligomers by cross-linking W^{HeV} $C^{all}S$ using DTSSP (**Supplementary Figure 3**). Upon crosslinking, W^{HeV} $C^{all}S$ was found to be remarkably soluble during the aggregation measurements (**Supplementary Figure 3A**), to strongly bind ThT (**Supplementary Figure 3B**) and to fibrillate after 2h of incubation (**Supplementary Figure 3C**). Because the DTSSP crosslinker contains a disulfide bridge, we added DTT to reduce the W^{HeV} $C^{all}S$ artificial oligomers to release free monomers before urea removal. The reduced sample still contains residual amounts of oligomers as observed in the SEC profile (**Supplementary Figure 3C**, inset) and showed, as expected, a lower solubility, but not as much as the non-cross-linked variant (**Supplementary Figure 3A**). Noteworthy, the reduced sample still strongly binds ThT (**Supplementary Figure 3B**) and NS-EM micrographs exhibited fewer though longer fibrils compared to those obtained in the absence of DTT (**Supplementary Figure 3C**). These results highlight a balance between fibril nucleation, dependent on W^{HeV} oligomers, and fibril elongation, dependent on the addition of free monomers.

Finally, we produced dimeric species by generating a protein construct (FKBP-$C^{all}S$) whose dimerization can be chemically induced (**Figure 3D-G**). FKBP-$C^{all}S$ was made by fusing W^{HeV} $C^{all}S$ and FK506-binding protein, FKBP. FKBP is a widely-used system to study homodimerization processes since the protein strongly dimerizes in the presence of the AP20187 molecule (24). FKBP-$C^{all}S$ is expected to be unable to fibrillate in the absence of AP20187, while the addition of the latter should promote the nucleation of fibrils *via* the formation of a large amount of chemically-induced dimeric species. After 10 minutes of incubation in the presence of AP20187, analysis of FKBP-$C^{all}S$ by SEC-MALLS showed that the chimeric protein was effectively predominantly dimeric (**Figure 3D**). Urea and unbound AP20187 were removed and the aggregation and binding to ThT were monitored for 2h (**Figure 3E** and **3F**). In these experiments, and in line with expectations, FKBP-$C^{all}S$ turned out to be more soluble and to bind ThT to a higher extent in the presence of AP20187 than in its absence (**Figure 3E** and **3F**). In the absence of AP20187, the protein slightly binds ThT, an observation that can be accounted for by the initial presence of low amounts of dimeric species in the purified sample. Consequently, a very small number of very short fibrils was observed without AP20187, while their number greatly increased in its presence (**Figure 3G**). Because of the large molar excess of AP20187 used in these experiments, dimerization is strongly promoted. Because of the very low amounts of monomers, fibril nucleation is strongly favored at the expense of elongation, resulting in numerous and very short fibrils (**Figure 3G**).

Taken together, these observations demonstrate that W^{HeV} dimerization is the driver of the nucleation process and represents a critical step in the formation of amyloid-like fibrils. A similar conclusion can be drawn for W^{NiV} owing to the correlation between the W^{NiV} oligomers proportion and its nucleation extent (see **Figure 1**).

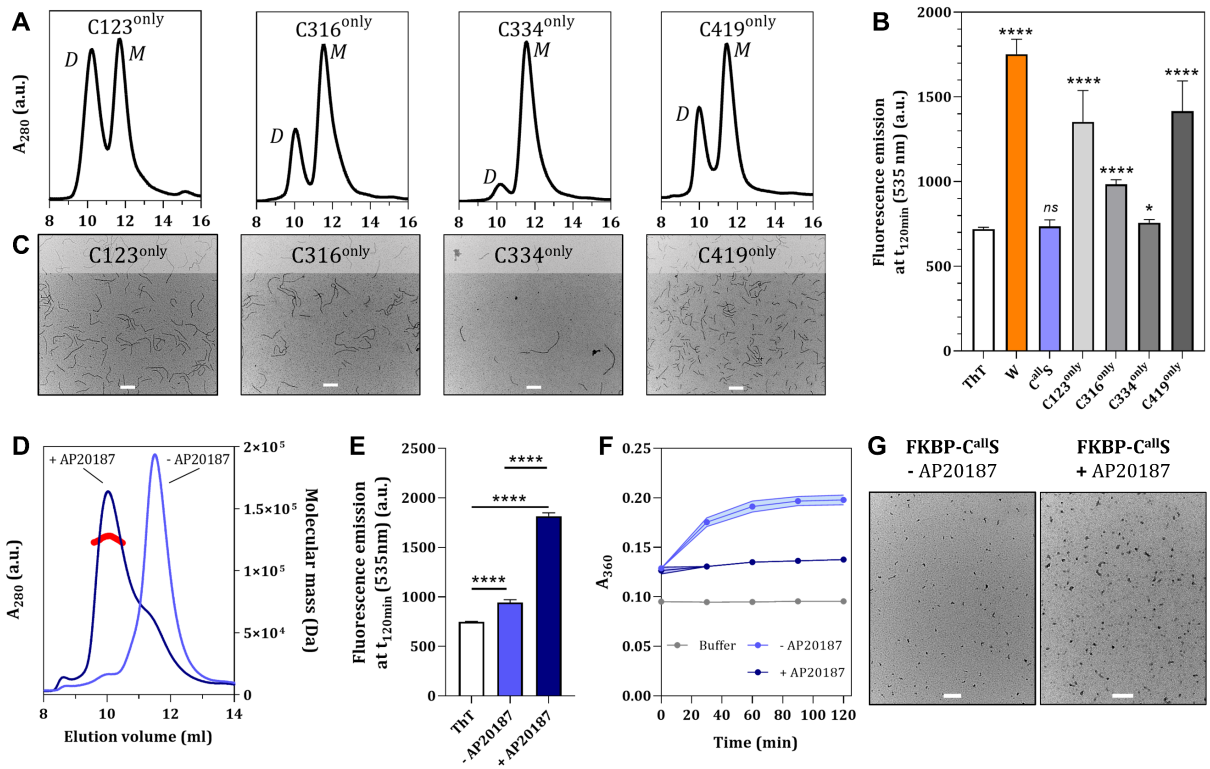

Figure 3. W^{HeV} dimerization is sufficient to promote fibrillation. A) Analytical SEC of W^{HeV} with triple Cys to Ser substitutions preincubated 48h in urea. M and D stand for monomeric and dimeric species, respectively. **B)** ThT fluorescence measurements of W^{HeV} triple variants, preincubated in urea for 48h, after 2h in urea-free buffer. Shown are mean values and s.d. as obtained from n ≥ 4 independent measurements. Panel B also shows the fluorescence of ThT alone (white) and of W^{HeV} (orange) and W^{HeV} $C^{all}S$ (blue) for comparison. Statistical analyses were performed using the Student t-test, comparing fluorescence data to those obtained with ThT alone. **C)** NS-EM micrographs of W^{HeV} with triple Cys to Ser after 2h of incubation following urea removal. Scale bar: 200 µm. **D)** Analytical SEC of FKBP-$C^{all}S$ in the presence (dark blue) or absence (light blue) of the AP20187 molecule along with the molecular mass determination by SEC-MALLS of FKBP-W^{HeV} $C^{all}S$ in the presence of AP20187 (127 800 Da, red). Turbidimetry **(E)** and ThT fluorescence measurements **(F)** of FKBP-W^{HeV} $C^{all}S$ preincubated (dark blue) or not (light blue) with AP20187. Panel E also shows the fluorescence of ThT alone (white). **G)** Micrographs of FKBP-$C^{all}S$ after 2 hours of incubation with or without AP20187. Panels B, E, and F show mean values and s.d. as obtained from n=4 independent measurements. The shaded region in F) corresponds to the error bar. Statistical analysis was made with a Student t-test; ns: not significant, ****: p<0.0001. Scale bar: 200 µm.

W^{HeV} forms redox-sensitive fibrillar structures in transfected cells

We next assessed the ability of W^{HeV} to fibrillate *in cellula*. To allow the visualization of W^{HeV} in living, *i.e.*, non-permeabilized cells, we generated constructs driving the eukaryotic expression of W^{HeV} fused to a tetracysteine (*tc*) peptide tag (25, 26) appended either at the N- (*tc*-W) or C-terminus of the protein (W-*tc*). HEK 293T cells were transfected with these constructs or an empty control plasmid, and W^{HeV} was detected by confocal microscopy after 24 or 48h post-transfection using the membrane-permeable ReAsH dye, which only fluoresces upon binding to the *tc* tag.

In some transfected cells expressing W^{HeV}, nuclear filamentous structures and aggregates could be observed both 24h and 48h post-transfection (**Figures 4A**, **B** and **Supplementary Figure 4**). Indeed, *tc* staining (red) was only visible in W^{HeV}-stained nuclei (magenta), confirming that the filaments were composed of W^{HeV} (**Figure 4A**, insets). These structures were not detectable in cells transfected with the empty vector, nor in cells expressing an irrelevant fluorescent protein (EGFP) (**Figure 4A**) thus ruling out the possibility of non-specific ReAsH binding. In spite of a very low

transfection efficiency, aggregates and filamentous nuclear structures were also detectable in human alveolar basal epithelial A549 cells (**Supplementary Figure 5**), a relevant cellular model for henipavirus infection. EM analysis of ultrathin sections of transfected HEK293 cells expressing W-*tc* at 24h post-transfection and displaying nuclear filamentous aggregates confirmed the presence of fibrillar structures. These structures were consistently observed at several heights along the *z* axis of the reference fluorescence stack (**Figures 4C** and **4D**, see Material and Methods and SI Appendix for details of the correlative approach). Similar structures were also observed at 48h post-transfection (**Supplementary Figure 6A**), while they were never observed in non-transfected cells (**Supplementary Figure 6B)**, nor in transfected cells in which no fibrillar structures could be detected by confocal microscopy (**Supplementary Figure 6C**).

Based on confocal microscopy acquisitions obtained with the *tc*-tagged W^{HeV} proteins over different Z optical sections, the tridimensional arrangement of the nuclear fibrils was reconstituted and revealed various morphologies of fibrils. Small, straight and flattened rod-like structures were observed. Different intermediates in several filament-positive nuclei, notably long and intertwined filaments invading a large area of the nucleus could be detected. We could also distinguish structures composed of a single or two filament(s), coiling and “looping” inside the nucleus. These different forms likely reflect distinct maturation stages of the fibrils, with the former corresponding to early-stage fibrils observed shortly after nucleation, and the latter to more elongated filaments having incorporated a large number of W monomers.

To assess the redox-dependence of the fibrillar aggregates formed by the W^{HeV} protein *in cellula*, HEK 293T cells were also transfected with constructs driving the expression of W^{HeV} $C^{all}S$ with either an N- (*tc*-$C^{all}S$) or a C-terminal ($C^{all}S$-*tc*) *tc* tag (**Figure 4A** and **4B**). Quantitative analysis revealed that replacing all the cysteine residues with serine (W^{HeV} $C^{all}S$ variant) induces a significative decrease of the number of cells with nuclear filaments in the case of the *tc*-$C^{all}S$ variant (**Figure 4E** and **Supplementary Table 2**). Filaments were found in similar amounts 24 and 48h post-transfection. Unexpectedly, *tc*-W is significantly more prone to form filaments compared to W-*tc* indicating that the *tc* tag interferes with the ability of W^{HeV} to fibrillate *in cellula* when present at the C-terminus of the protein. The expression level of W^{HeV} variants was verified by IF staining and appeared to be higher for *tc*-W^{HeV} compared to W^{HeV}-*tc* constructs (**Supplementary Figure 4**), a finding that can be regarded as another plausible explanation for the reduced fibrillation propensity of W^{HeV}-*tc* constructs. Importantly, no apparent difference in expression level was observed between W^{HeV} and the $C^{all}S$ variant (**Supplementary Figure 4**), thus ruling out the possibility that the observed differences could merely reflect differences in expression levels. Of note, although W^{HeV} has some toxic effect in HEK293T cells, no difference in cell viability were observed between the various W^{HeV} variants (**Supplementary Figure 7**). Altogether, these data indicate that W^{HeV} can give rise to filaments in cells and that this ability is impaired, or at least delayed, when the protein is devoid of cysteine residues consistent with their role in the nucleation of fibrils.

W expression induces reactive oxygen species production in transfected cells

Oxidative stress is a common feature during viral infections where mitochondria are targeted by viral proteins to promote a strong production of reactive oxygen species (ROS) (27), with this being also true in the case of NiV (28). As such, henipavirus infection would generate an environment favorable for the production of W fibrils. Since those fibrils could be detected in the nuclei of transfected cells, we expected transfection and/or expression of the W protein to mimic infection and to be able to trigger the production of ROS, thereby enabling ensuing fibril formation. Quantification of ROS by confocal microscopy in HEK293T cells transfected with an empty vector or W constructs showed that expression of W^{HeV} did significantly induce ROS production (**Figures 5A**, **5B** and **Supplementary Table 2**), thus confirming our expectations. The increase in ROS triggered by W would create an oxidative environment favoring the formation of fibrils.

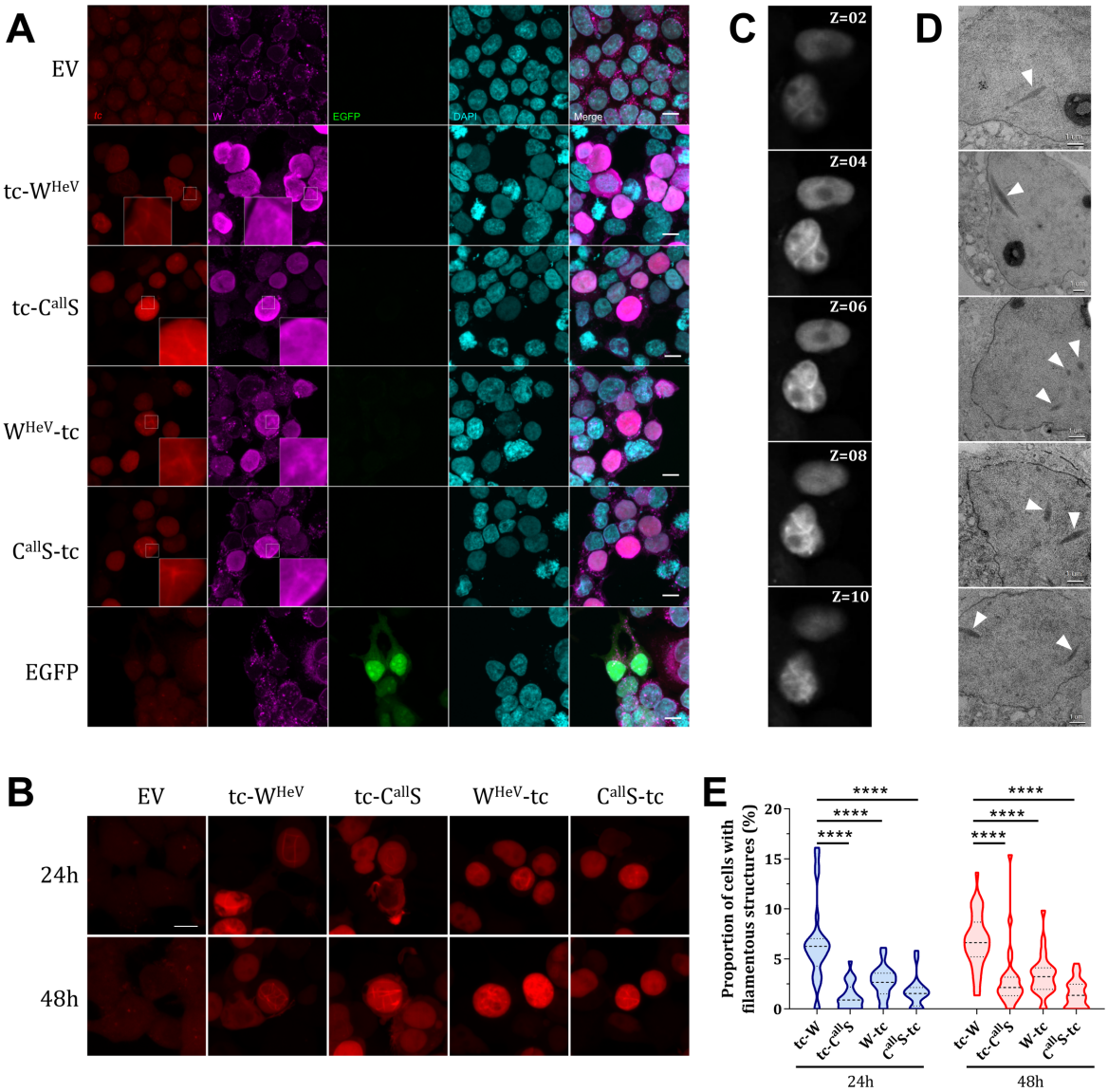

Figure 4. W^{HeV} forms redox-sensitive filamentous structures *in cellula*. A) Confocal microscopy analysis of HEK293T cells transfected with either an empty vector (EV), or enhanced green fluorescent protein (EGFP), or the indicated tetracysteine (*tc*)-tagged W^{HeV} constructs. W^{HeV} filaments were visualized 24h post-transfection with ReAsH dye to detect the *tc* peptide (red) and immunofluorescence staining targeting W^{HeV} (violet). Nuclei were counterstained with DAPI (blue). Scale bar, 10 µm. **B)** Z-stack projections of live HEK293T cells transfected with an empty vector or the indicated tetracysteine (*tc*)-tagged W^{HeV} constructs. Cells were stained 24h and 48h post-transfection with ReAsH dye to detect the *tc* peptide and imaged by confocal microscopy. Images are representative of three independent experiments. Scale bar, 10 µm. **C)** Z-stack projections of HEK293T cells transfected with a construct driving the expression of W^{HeV} with a C-terminal *tc* tag 24h post-transfection. Cells were stained and imaged as described in panel B. **D)** Electron micrographs of ultrathin sections at equivalent Z positions of the cells shown in C). The arrowheads indicate the fibrillar structures detected in the nuclei of the transfected cells. **E)** Quantification of the percentage of cells with filaments. Cells with filaments were counted from the Z-projections. Data are expressed as mean ± sd and are representative of three independent experiments with $n \geq 19$ for each condition. Statistical significance was assessed with two-way ANOVA completed with a Tukey's multiple comparison test. ****$p < 0.0001$.

W-mediated repression of NF-κB pathway is impaired in the W^{HeV} $C^{all}S$ variant

W proteins interact with multiple innate immune host factors to counteract the antiviral response, *e.g.*, they inhibit NF-κB pathway activation *via* sequestration of 14-3-3 into the nucleus as we recently reported (16, 20). We thus focused on the NF-κB pathway in our quest of fibril functional impact.

To this end, we took advantage of a HEK293 cell line stably expressing a firefly luciferase reporter under the control of a synthetic NF-κB promoter (HEK293- NF-κB_luc), as a proxy for NF-κB pathway activity as already described (29). We transfected these cells with constructs driving the expression of *tc*-W or *tc*-$C^{all}S$. Only N-terminally *tc* tagged constructs were used in these experiments to avoid any possible interference of the tag with CTD-mediated binding to 14-3-3 proteins. We used the same Flag-W^{NiV} construct as the one formerly used (20) as a positive control. Basal luciferase activity was significantly reduced in both W^{HeV} and W^{NiV}-expressing cells (**Figure 5C**). Strong luciferase expression induced by IL-1β treatment was significantly inhibited in cells transfected with W^{HeV} and W^{NiV}, while inhibition was found to be attenuated for the $C^{all}S$ variant (**Figure 5C**). Specifically, NF-κB activity was significantly higher for *tc*-$C^{all}S$ compared to its wild-type counterpart. These results mirror the propensity of the different W constructs to fibrillate, with *tc*-W^{HeV} being highly fibrillogenic and *tc*-$C^{all}S$ displaying a highly impaired ability to fibrillate (**Figure 4E**).

Although the nuclear localization of W proteins is well established, they undergo nucleocytoplasmic trafficking and can thus be occasionally found in the cytoplasm (30). This shuttling property was checked for all W^{HeV} variants to ensure neither the *tc* tag nor the cysteine substitutions were impairing the protein trafficking. Confocal microscopy analysis showed that all the variants display comparable nucleo-cytoplasmic distribution suggesting that the shuttling was not affected (**Supplementary Figures 4B** and **4C**). Altogether, these observations suggest that the W-mediated inhibition of the NF-κB pathway is associated to the ability of W^{HeV} to fibrillate and not on its sole presence as a monomeric protein nor on a possible impairment of W nucleocytoplasmic shuttling brought by the $C^{all}S$ substitution and/or by the *tc* tag.

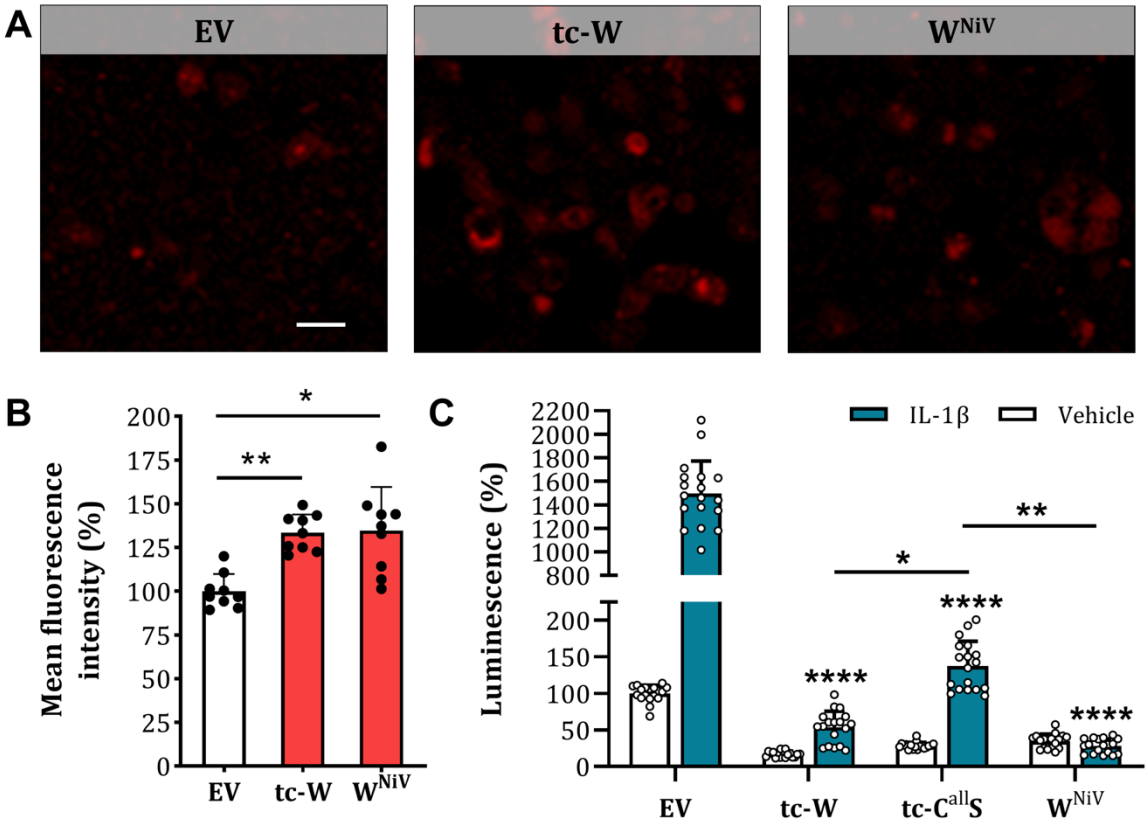

Figure 5. W^{HeV} fibrils impact the NF-κB pathway and induce ROS production. A) Detection of intracellular ROS in W-transfected HEK293T cells at 24h post-transfection by confocal microscopy and **B)** Fluorescence intensity quantification for each condition. Data are expressed as mean ± sd (n = 9 fields of view). Statistical significance was assessed with the Kruskal-Wallis test completed by a Dunn's multiple comparison test. Only comparisons of interest are plotted. *p<0.05, **p < 0.01. **C**) Measurement of NF-κB activity in W-transfected cells. HEK293 NF-κB_luc cells were transfected with an empty vector (EV), *tc*-tagged W^{HeV} constructs, or FLAG-tagged W^{NiV}, stimulated (blue) or not (white) 24h later with 50 ng/ml IL-1β before assessing NF-κB activity by luminescence quantification. Data are expressed as mean ± sd and are representative of three independent experiments (n = 18). Statistical significance was assessed with two-way ANOVA completed with a Tukey's multiple comparison test. Asterisks above error bars denote significance compared to the corresponding EV condition. *p<0.05, ** p < 0.01, ****p < 0.0001.Scale bar: 20 µm.

Discussion

We herein report the crucial implication of cysteine residues in the fibrillation ability of the W protein both *in vitro* and *in cellula*. SEC analysis of W proteins preincubated for different periods under denaturing and oxidative conditions showed that they undergo disulfide bridge-mediated oligomerization. This process is closely related to W^{HeV} and W^{NiV} solubility since in the absence of disulfide-bridged oligomers, amorphous aggregates are formed, as shown by experiments in the presence of a reducing agent or using the W^{HeV} $C^{all}S$ variant. Similarly, oligomerization of both W was also found to be closely tied to the formation of amyloid-like fibrils and as such, oligomers represent the fundamental drivers of primary nucleation. In support of this hypothesis, the requirement for a single cysteine residue for fibril formation and the substantial increase in W^{HeV} $C^{all}S$ solubility and ability to form fibrils upon generation of chemically-induced dimers support the conclusion that dimeric species are the primary drivers of nucleation. Notably, those dimers can be formed through any cysteine residue, as judged from the fibrillation abilities of the $Cys123^{only}$, $Cys316^{only}$, $Cys334^{only}$ and $Cys419^{only}$ variants. Furthermore, dimers do not require to be disulfide bridged to promote nucleation as illustrated by the fibrillation abilities of the artificially induced $C^{all}S$ dimers as obtained *via* addition of AP20187 to FKBP-$C^{all}S$. Nucleation *via* disulfide-bridged dimers has been described in the case of Tau (31) and fish β-parvalbumin (32) while non-covalent dimers were shown to initiate nucleation for other proteins, such as the Aβ peptide (33) or α-synuclein (34, 35). However, unlike these latter proteins, the monomeric species of W^{HeV} and W^{NiV} are not stable in solution and rapidly aggregate. W^{HeV} and W^{NiV} disulfide-bridged oligomers seem to enable bypassing the lag phase that is usually observed during the amyloidogenesis process (36) through the formation of covalent oligomers that eventually polymerize. Interestingly, mature W^{HeV} and W^{NiV} fibrils are not completely sensitive to reduction, indicating that a successive and distinct stabilizing mechanism, presumably brought by the PNT3 region (residues 200-310) that is also present in W (37), is at play in the fibril elongation step compared to the initial nucleation step.

Another consequence of the presence of multiple Cys in W^{HeV} is the formation of intrachain disulfide bonds, which decreases the hydrodynamic radius of the monomer. This compact conformation is not required for W^{HeV} fibrillation as shown by the Cys^{only} W^{HeV} variants. On the contrary, intrachain disulfide bonds may impair the fibrillation process by decreasing the nucleation extent since less cysteine residues are available to establish an interchain bridge. This scenario is in agreement with previous observations on other amyloidogenic proteins, where increasing the compaction of α-synuclein *via* the addition of an artificial disulfide bond strongly decreases its fibrillation propensity (38, 39). Similarly, intrachain disulfide bonds in 4R Tau isoforms cause the formation of compact monomers that are not able to fibrillate (31). According to our observations, the probable functions of cysteine residues are 1) to allow monomers to dimerize, enabling fibril nucleation, 2) to maintain them soluble and 3) to prevent fibril clustering.

Interestingly, we were able to document the formation of fibrillar structures in a cellular context using a tetracysteine tag, already employed in (40). This ability is impaired in the $C^{all}S$ variant, a finding in line with the ensemble of data obtained *in vitro* with purified proteins. W^{HeV} fibrils were exclusively found in the nucleus of transfected cells and in a limited number. The formation of fibrils under non-reducing conditions raises the question of the ability of W proteins to fibrillate *in vivo* since the nucleus and the cytosol are reducing environments. Noteworthy, NiV infection induces ROS production (28), and we showed that the sole ectopic expression of W^{HeV} resulted in the production of ROS thereby creating an environment favorable to fibril formation and eventually provoking and/or amplifying the nuclear fibrillogenesis of W. These observations are in line with several studies on various proteins with fibrillogenic potential. The human protein $p16^{INK4A}$ that only fibrillates when its unique cysteine is oxidized, was shown to fibrillate in cultured cells under mild oxidizing conditions (41). Likewise, disulfide bond-dependent viral amyloids made by the NSs protein from the Rift Valley fever virus could be observed in both transfected and infected cells (40). These two examples, together with the ones herein presented, indicate that the oxidation of cysteine

residues shown to be critical for fibril formation does take place in the cellular context. Our experimental data therefore strongly support the ability of the W protein to fibrillate *in cellula*.

As previously described (20), W^{NiV} CTD binds and accumulates 14-3-3 into the nucleus leading to an increased cytosolic translocation of NF-κB p65/p50 and consequently a reduced expression of proinflammatory cytokines. Our study confirms and extends these findings: not only it shows that the W^{HeV} protein is able to impair the NF-κB pathway, but also it provides evidence for an enhancing effect mediated by fibrils. Indeed, the formation of amyloid-like fibrils was shown to augment this ability compared to the monomeric protein, as judged from the observation that the NF-κB pathway is less impaired with the $C^{all}S$ variant that forms fewer fibrils *in cellula* than its *wild-type* counterpart.

In conclusion, the present study constitutes the first experimental evidence of the ability of the *Henipavirus* W proteins to also form fibrils in a cellular context. Although other possible mechanisms cannot be ruled out, by establishing a functional link between fibril formation and impairment of the NF-κB pathway, this study provides the first clues on the functional impact of fibrils thus shedding light on the possible molecular mechanisms by which these virulence factors may contribute to *Henipavirus* pathogenesis. Further studies will explore to which extent the W assembly into fibrils participate to W function during *Henipavirus* infection *in cellula* and *in vivo*. The quick formation of W fibrils may benefit to the virus to fight against the cell innate immune response in light of the short timescale of viral infections, the duration of which is limited to few hours *in vitro* (43) and few days *in vivo* after experimental infection (44). Viral amyloids represent a new promising antiviral target considering their emerging roles in virus replication (45). Work is currently in progress to unravel the functional impact of fibril formation by the W^{HeV} protein in animals by taking advantage of the availability of a non-fibrillogenic W variant.

Acknowledgments

We acknowledge the PICsL-FBI electron microscopy facility of the IBDM, members of the national infrastructure France-BioImaging supported by the French National Research Agency (ANR-10-INBS-04), for providing access and thank Fabrice Richard for his technical help. We also acknowledge the mass spectrometry facility of Marseille Proteomics (marseille-proteomique.univ-amu.fr), supported by IBISA (Infrastructures Biologie Santé et Agronomie), Plateforme Technologique Aix-Marseille, the Cancéropôle PACA, Région Sud-Alpes-Côte d'Azur, the Institut Paoli-Calmettes, the Centre de Recherche en Cancérologie de Marseille (CRCM), Fonds Européen de Développement Régional and Plan Cancer. We thank María Jesús Maté for the SEC-MALLS experiments. We thank all the AFMB technical and support staff (Denis Patrat, Patricia Clamecy, Béatrice Rolland, Paul Zamboni, Chantal Falaschi and Fabienne Amalfitano). We also thank Joanna Brunel who build the parental plasmid encoding FKBP from synthetic gene constructs and finally Racha Majed (Refeyn company) for the mass photometry measurements. We acknowledge the contribution of SFR Biosciences (UAR3444/CNRS, US8/Inserm, ENS de Lyon, UCBL) facility Plateau Technique d'Imagerie/Microcopie (PLATIM).

Materials and Methods

Generation of constructs

The generation of the constructs is detailed in the **SI Appendix, Materials and Methods** (see **Supplementary Tables 3** and **4**). The resulting constructs for bacterial and eukaryotic expression allow the expression of 6-His tagged recombinant proteins, and N- or C-terminally *tc*-tagged proteins, respectively.

Expression and purification of recombinant proteins

Expression of all recombinant proteins was made in the *E. coli* strain T7pRos. The detailed protocol for proteins expression and purification is detailed in the **SI Appendix, Materials and Methods**. Briefly, recombinant W proteins and their variants were purified in denaturing and reductive conditions (*i.e.* in presence of 6 M urea and of DTT) by Ni-NTA affinity chromatography and anion exchange chromatography (AEC). Protein samples were then desalted to remove the DTT and stored at -80°C in denaturing conditions. FKBP- $C^{all}S$ was purified in the same way except that an additional preparative SEC was performed in HBS/1 M urea. Purified proteins analyzed by SDS-PAGE are presented in **Supplementary Figure 8**.

Protein sequencing by tandem mass spectrometry

The identity of the compact conformation of W^{HeV} was confirmed by mass spectrometry analysis of tryptic fragments obtained after digestion of the purified protein band excised from SDS-polyacrylamide gel. The detailed protocol is further described in **SI Appendix, Materials and Methods**.

Analytical SEC of non-incubated and incubated proteins

One hundred µL of W^{HeV} (wild-type and variants) or W^{NiV} (wild-type) samples at 75 µM in HBS/6 M urea buffer, incubated at 37°C without agitation for different times, were injected onto a Superdex S200 Increase 10/300 GL (Cytiva) column equilibrated in HBS and eluted in the same buffer at a flow rate of 0.8 mL/min and at room temperature.

Mass photometry measurements

Mass photometry experiments were carried out on a TwoMP mass photometer (Refeyn). Wild-type W^{HeV} was incubated at a final concentration of 75 µM for 48h at 37°C and then diluted to 100 nM in HBS for molecular mass measurements.

Turbidimetry and fluorimetry measurements

Protein samples were incubated at 37°C for different times (indicated in each experiment) as detailed in the **SI Appendix, Materials and Methods**. Proteins solutions were then buffer exchanged to remove urea. The resulting urea-free protein samples were analyzed in the presence of thioflavin T (ThT). Turbidity measurements and fluorescence measurements were performed on a Tecan microplate reader GENios Plus in black 96-well plates with transparent flat bottom (Greiner, 655096) incubated at 37°C.

The same protocol was followed in the experiments made in the presence of DTT. 2 mM DTT was added either just after the buffer exchange step (t_0), or on a W^{HeV} sample that had already been incubated for two hours (t_{2h}). In this latter case, turbidity and fluorescence were monitored for two extra hours ($t_{2h + 2h}$). This latter sample was further incubated at 37°C for a total of 24h and then centrifuged at 10 000 x g for 10 min. The pellet was resuspended in 150 µL of HBS before being deposited on a NS-EM grid.

Measurements were performed at least in triplicate (indicated in each experiment) and data are represented as mean ± standard deviation (s.d.). The statistical analysis used is detailed for each

experiment, using either a one-way ANOVA with the Dunnett's multiple comparison test, or a Student's t-test.

Negative-staining electron microscopy (NS-EM)

NS-EM carbon coated grids were prepared from proteins samples incubated for 120 min at 37°C in HBS. A final concentration of 2 µM was used to this purpose as detailed in the **SI Appendix, Materials and Methods**. Measurements of fibrils lengths were made manually with the ImageJ software (46).

Chemically-induced dimerization of FKBP-C^{all}S

FKBP-C^{all}S sample was incubated in the absence or presence of AP20187 (Sigma-Aldrich, SML2838) as detailed in the **SI Appendix, Materials and Methods**. A part of the sample was analyzed by SEC and excess AP20187 was remove using a PD Minitrap G-25 column (Cytiva) equilibrated in HBS. Buffer exchanged samples were analyzed by turbidity and fluorimetry and NS-EM in the same way as described above.

Multi-angle laser-light scattering (SEC-MALLS)

The formation of FKBP-C^{all}S dimeric species upon addition of the AP20187 molecule was also assessed by SEC-MALLS. For this purpose, the same protocol as previously described was followed and the sample was centrifuged for 15 min at 10 000 x g at room temperature. 50 µL were injected at a flow rate of 0.6 mL/min on a Superdex S200 Increase 10/300 GL (Cytiva) column equilibrated in HBS controlled by an Ultimate 3000 HPLC (Thermo Scientific). Measurements were carried out on a Wyatt Dawn 8 angles MALLS equipped with an Optilab refractometer (Wyatt).

W^{HeV} C^{all}S variant crosslinking by DTSSP

W^{HeV} C^{all}S was cross-linked in the presence of 2 mM DTSSP (Pierce, 21578). The entire protocol is described in the **SI Appendix, Materials and Methods**. Half of the solution was reduced, while the other half was not reduced. Both solutions (reduced and unreduced) were analyzed by SEC and by turbidimetry and fluorimetry after a buffer-exchange step in HBS, as described above, at a final concentration of 30 µM. NS-EM grids were prepared after 2h of incubation in HBS.

Cellular cultures

Human embryonic kidney 293T (HEK293T), A549 and the HEK293 cell line stably transduced with a firefly luciferase reporter under the control of a synthetic NF-κB promoter (HEK293-NF-κB_luc, BPS-Bioscience) were cultured in Dulbecco's Modified Eagle Medium (DMEM) (Gibco, Cat# 61965-026) supplemented with 10 % fetal calf serum at 37 °C in a 5 % CO_2 incubator.

Immunofluorescence

Transfected HEK293T cells were stained using standard immunofluorescence protocol detailed in the **SI Appendix, Materials and Methods**, using a rabbit anti-W^{CTD} antibody (GeneScript) (1:100) and Alexa Fluor 647 Donkey anti-Rabbit IgG (H+L) Highly Cross-Adsorbed Secondary antibody (Invitrogen, Cat# A-31573) (1:500), before imaging on a Yokogawa HCS CQ1 confocal system (PLATIM, SFR Biosciences Lyon). Analysis of W^{HeV} cellular localization was performed using Fiji (v2.9.0), by counting semi-automatically the total number of cells in the DAPI channel. The number of cells with the different W^{HeV} expression profiles were counted manually.

Live imaging and quantification of W^{HeV} filaments

Transfected HEK293T and A549 cells were imaged using the TC-ReAsH™ II In-Cell Tetracysteine Tag Detection Kit. The ReAsH-EDT2 labeling reagent was used at a final concentration of 2.5 µM, allowing the visualization of *tc*-tagged W^{HeV} on a Yokogawa HCS CQ1 confocal system. Z-stacks of 10-µm-range with an imaging step of 0.7-1 µm were acquired in random areas of the wells. Quantification of the percentage of cells bearing filaments was performed with Fiji (v2.9.0). For each

condition, at least 19 projections were quantified, and shown data are representative of three independent experiments.

3D modeling of filament-bearing nuclei

Z-stacks of nuclei of transfected HEK293T cells with filaments were generated using Fiji, and the 3D Projection function was then used to create the 3D rendering, with the 'Brightest Point' projection method, the 'Slice spacing' parameter corresponding to the Z step of the microscopy acquisition, and the 'Interpolate' option checked.

Preparation of samples for electron microscopy of transfected cells

Transfected HEK293T cells were imaged using the TC-ReAsH™ II In-Cell Tetracysteine Tag Detection Kit on a Yokogawa HCS CQ1 confocal system to locate filament-bearing cells. After imaging, cells were fixed with 4 % methanol-free formaldehyde (Electron Microscopy Sciences, Cat# 15713) for 10 min, and kept in DPBS before tomography analysis.

Embedding and ultramicrotomy of transfected cells, and EM analyses

HEK293T cells were prepared following a regular EM sample preparation detailed in the **SI Appendix, Materials and Methods**. Briefly, cells were post-fixed in 1% OsO_4, *en bloc* contrasted in 1% uranyl acetate, dehydrated in ethanol and embedded in Epon. The region of interest was recovered from the dish and targeted using Ibidi landmarks. One-micron thick sections were collected on a glass slide. Sections of interest (those corresponding to the relevant z-positions in the fluorescence stacks) were identified by toluidine blue staining and re-embedded in pure Epon 812 and incubated at 60°C for approximately 12 hours. The samples were then immersed in liquid nitrogen to remove the resin-embedded sections from the slide (cracking). 70-90 nm ultrathin sections were post-stained with uranyl acetate and lead citrate. Images were taken using a Tecnai™ T12 Spirit 120 kV.

Luciferase assay

HEK293 NF-κB_luc cells were transfected with an empty pcDNA3.1(+) vector, pcDNA3.1(+) plasmids coding for *tc*-tagged W^{HeV} variants or pCG-FLAG-NiV-W plasmid. Medium was replaced 24 h later with DMEM-10% FCS supplemented or not with 50 ng/ml human IL-1β (PeproTech, 200-01B). Luciferase activity was measured 5 h later using Bright-Glo Luciferase Assay System (Promega, E2620) on a Tristar 5 microplate reader (Berthold).

Intracellular ROS quantification

Intracellular ROS were quantified in transfected HEK293T cells using the Fluorometric Intracellular ROS Kit (Sigma-Aldrich, MAK145). Cells were imaged on a Yokogawa HCS CQ1 confocal microscope. For each condition, single optical sections from nine random areas in the wells were acquired. Images were then analyzed with Fiji (v2.9.0), by first subtracting the background (rolling ball radius of 50 pixels) and then measuring the mean gray value was for each field of view.

Cell viability assay

Viability of transfected HEK293T cells was measured 24 h post-transfection using alamarBlue Cell Viability Reagent (Invitrogen, DAL1025) by quantifying fluorescence intensity on a Tristar 5 microplate reader, using an excitation wavelength of 570 ± 7.5 nm, an emission wavelength of 585 ± 7.5 nm, and an exposure time of 100 ms.

Funding

This work was carried out with the financial support of the Agence Nationale de la Recherche (ANR), specific project Heniphase (ANR-21-CE11- 0012-01) that was labeled by the Eurobiomed and Lyon Biopole competitiveness clusters. It was also partly supported by the CNRS and by the French Infrastructure for Integrated Structural Biology (FRISBI) (ANR-10-INSB-0005). F.G. is

supported by a post-doctoral fellowship from the FRM (Fondation pour la Recherche Médicale). G.P. is supported by a joint doctoral fellowship from the AID (Agence Innovation Défense) and Aix-Marseille University (AMU).

References

1. J. Quarleri, V. Galvan, M. V. Delpino, Henipaviruses: an expanding global public health concern? *GeroScience*, 1–13 (2022).
2. B. Escudero-Pérez, A. Lalande, C. Mathieu, P. Lawrence, Host-Pathogen Interactions Influencing Zoonotic Spillover Potential and Transmission in Humans. *Viruses* **15**, 599 (2023).
3. G. A. Marsh, *et al.*, Cedar virus: a novel Henipavirus isolated from Australian bats. *PLoS Pathog* **8**, e1002836 (2012).
4. S. Mallapaty, New "Langya" virus identified in China: what scientists know so far. *Nature* **608**, 656–657 (2022).
5. R. Amin, R. Darwin, H. Chopra, T. B. Emran, Langya virus: Slope of the iceberg for unexplored pathogens. *Int J Surg* **109**, 163–164 (2023).
6. S.-H. Lee, *et al.*, Discovery and Genetic Characterization of Novel Paramyxoviruses Related to the Genus Henipavirus in Crocidura Species in the Republic of Korea. *Viruses* **13**, 2020 (2021).
7. B. E. Dawes, A. N. Freiberg, Henipavirus infection of the central nervous system. *Pathog Dis* **77**, ftz023 (2019).
8. B. Nikolay, *et al.*, Transmission of Nipah Virus - 14 Years of Investigations in Bangladesh. *N Engl J Med* **380**, 1804–1814 (2019).
9. R. Gómez Román, *et al.*, Medical countermeasures against henipaviruses: a review and public health perspective. *Lancet Infect Dis* **22**, e13–e27 (2022).
10. M. L. Shaw, Henipaviruses Employ a Multifaceted Approach to Evade the Antiviral Interferon Response. *Viruses* **1**, 1190–1203 (2009).
11. K. M. Smith, *et al.*, Structural basis for importin alpha 3 specificity of W proteins in Hendra and Nipah viruses. *Nat Commun* **9**, 3703 (2018).
12. M. K. Lo, *et al.*, Determination of the henipavirus phosphoprotein gene mRNA editing frequencies and detection of the C, V and W proteins of Nipah virus in virus-infected cells. *J Gen Virol* **90**, 398–404 (2009).
13. J. J. Rodriguez, J.-P. Parisien, C. M. Horvath, Nipah Virus V Protein Evades Alpha and Gamma Interferons by Preventing STAT1 and STAT2 Activation and Nuclear Accumulation. *J Virol* **76**, 11476–11483 (2002).
14. S. Tsimbalyuk, *et al.*, The Intrinsically Disordered W Protein Is Multifunctional during Henipavirus Infection, Disrupting Host Signalling Pathways and Nuclear Import. *Cells* **9**, E1913 (2020).
15. C. F. Basler, Nipah and hendra virus interactions with the innate immune system. *Curr Top Microbiol Immunol* **359**, 123–152 (2012).
16. F. Gondelaud, *et al.*, Functional benefit of structural disorder for the replication of measles, Nipah and Hendra viruses. *Essays Biochem*, EBC20220045 (2022).
17. C. Wang, *et al.*, Evasion of Host Antiviral Innate Immunity by Paramyxovirus Accessory Proteins. *Frontiers in Microbiology* **12** (2022).
18. E. D. Laing, *et al.*, Rescue and characterization of recombinant cedar virus, a non-pathogenic Henipavirus species. *Virol J* **15**, 56 (2018).
19. M. L. Shaw, A. García-Sastre, P. Palese, C. F. Basler, Nipah virus V and W proteins have a common STAT1-binding domain yet inhibit STAT1 activation from the cytoplasmic and nuclear compartments, respectively. *J Virol* **78**, 5633–5641 (2004).
20. F. Enchéry, *et al.*, Nipah virus W protein harnesses nuclear 14-3-3 to inhibit NF-κB-induced proinflammatory response. *Commun Biol* **4**, 1–15 (2021).

21. M. R. Edwards, *et al.*, Henipavirus W Proteins Interact with 14-3-3 To Modulate Host Gene Expression. *J Virol* **94**, e00373-20 (2020).
22. G. Pesce, *et al.*, Experimental Evidence of Intrinsic Disorder and Amyloid Formation by the Henipavirus W Proteins. *Int J Mol Sci* **23**, 923 (2022).
23. W. Liu, *et al.*, IBS: an illustrator for the presentation and visualization of biological sequences. *Bioinformatics* **31**, 3359–3361 (2015).
24. R. DeRose, T. Miyamoto, T. Inoue, Manipulating signaling at will: chemically-inducible dimerization (CID) techniques resolve problems in cell biology. *Pflugers Arch* **465**, 409–417 (2013).
25. B. R. Martin, B. N. G. Giepmans, S. R. Adams, R. Y. Tsien, Mammalian cell-based optimization of the biarsenical-binding tetracysteine motif for improved fluorescence and affinity. *Nat Biotechnol* **23**, 1308–1314 (2005).
26. N. J. Arhel, P. Charneau, Bisarsenical labeling of HIV-1 for real-time fluorescence microscopy. *Methods Mol Biol* **485**, 151–159 (2009).
27. J. Foo, G. Bellot, S. Pervaiz, S. Alonso, Mitochondria-mediated oxidative stress during viral infection. *Trends Microbiol* **30**, 679–692 (2022).
28. O. Escaffre, H. Halliday, V. Borisevich, A. Casola, B. Rockx, Oxidative stress in Nipah virus-infected human small airway epithelial cells. *J Gen Virol* **96**, 2961–2970 (2015).
29. S. Pène, L. Waast, A. Bonnet, L. Bénit, C. Pique, A non-SUMOylated tax protein is still functional for NF-κB pathway activation. *J Virol* **88**, 10655–10661 (2014).
30. M. D. Audsley, D. A. Jans, G. W. Moseley, Nucleocytoplasmic trafficking of Nipah virus W protein involves multiple discrete interactions with the nuclear import and export machinery. *Biochem Biophys Res Commun* **479**, 429–433 (2016).
31. B. Nizynski, W. Dzwolak, K. Nieznanski, Amyloidogenesis of Tau protein. *Protein Sci* **26**, 2126–2150 (2017).
32. T. E. R. Werner, D. Bernson, E. K. Esbjörner, S. Rocha, P. Wittung-Stafshede, Amyloid formation of fish β-parvalbumin involves primary nucleation triggered by disulfide-bridged protein dimers. *Proceedings of the National Academy of Sciences* **117**, 27997–28004 (2020).
33. O. Press-Sandler, Y. Miller, Distinct Primary Nucleation of Polymorphic Aβ Dimers Yields to Distinguished Fibrillation Pathways. *ACS Chem Neurosci* **10**, 4407–4413 (2019).
34. S. Lan-Mark, Y. Miller, Insights into the Interactions that Trigger the Primary Nucleation of Polymorphic α-Synuclein Dimers. *ACS Chem. Neurosci.* **13**, 370–378 (2022).
35. Y. Zhang, *et al.*, Molecular Insights into the Misfolding and Dimerization Dynamics of the Full-Length α-Synuclein from Atomistic Discrete Molecular Dynamics Simulations. *ACS Chem Neurosci* **13**, 3126–3137 (2022).
36. Z. Alraawi, N. Banerjee, S. Mohanty, T. K. S. Kumar, Amyloidogenesis: What Do We Know So Far? *International Journal of Molecular Sciences* **23**, 13970 (2022).
37. E. Salladini, *et al.*, Identification of a Region in the Common Amino-terminal Domain of Hendra Virus P, V, and W Proteins Responsible for Phase Transition and Amyloid Formation. *Biomolecules* **11**, 1324 (2021).
38. A. Carija, *et al.*, Biasing the native α-synuclein conformational ensemble towards compact states abolishes aggregation and neurotoxicity. *Redox Biol* **22**, 101135 (2019).
39. F. Pinheiro, S. Ventura, Inducing α-synuclein compaction: a new strategy for inhibiting α-synuclein aggregation? *Neural Regeneration Research* **14**, 1897 (2019).
40. P. Léger, *et al.*, NSs amyloid formation is associated with the virulence of Rift Valley fever virus in mice. *Nat Commun* **11**, 3281 (2020).
41. C. Göbl, *et al.*, Cysteine oxidation triggers amyloid fibril formation of the tumor suppressor p16INK4A. *Redox Biol* **28**, 101316 (2020).
42. A. K. Gardino, S. J. Smerdon, M. B. Yaffe, Structural determinants of 14-3-3 binding specificities and regulation of subcellular localization of 14-3-3-ligand complexes: a comparison of the X-ray crystal structures of all human 14-3-3 isoforms. *Semin Cancer Biol* **16**, 173–182 (2006).

43. G. A. Marsh, *et al.*, Recombinant Hendra viruses expressing a reporter gene retain pathogenicity in ferrets. *Virol J* **10**, 95 (2013).
44. V. Guillaume, *et al.*, Acute Hendra virus infection: Analysis of the pathogenesis and passive antibody protection in the hamster model. *Virology* **387**, 459–465 (2009).
45. F. Gondelaud, P.-Y. Lozach, S. Longhi, Viral amyloids: New opportunities for antiviral therapeutic strategies. *Curr Opin Struct Biol* **83**, 102706 (2023).
46. C. A. Schneider, W. S. Rasband, K. W. Eliceiri, NIH Image to ImageJ: 25 years of image analysis. *Nat Methods* **9**, 671–675 (2012).
47. A. Gruet, *et al.*, Fuzzy regions in an intrinsically disordered protein impair protein-protein interactions. *FEBS J* **283**, 576–594 (2016).
48. R. Vincentelli, *et al.*, High-throughput automated refolding screening of inclusion bodies. *Protein Sci* **13**, 2782–2792 (2004).